

High-resolution near-infrared speckle interferometry and radiative transfer modeling of the OH/IR star OH 104.9+2.4[★]

D. Riechers¹, Y. Balega², T. Driebe¹, K.-H. Hofmann¹, A. B. Men'shchikov^{1,3}, and G. Weigelt¹

¹ Max-Planck-Institut für Radioastronomie, Auf dem Hügel 69, 53121 Bonn, Germany
e-mail: [riechers;driebe;weigelt]@mpifr-bonn.mpg.de

² Special Astrophysical Observatory, Nizhnij Arkhyz, Zelenchuk district, Karachai-Cherkessian Republic, Russia

³ Institute for Computational Astrophysics, Saint Mary's University, Halifax, Canada

Received 27 February 2004 / Accepted 18 May 2004

Abstract. We present near-infrared speckle interferometry of the OH/IR star OH 104.9+2.4 in the K' band obtained with the 6 m telescope of the Special Astrophysical Observatory (SAO). At a wavelength of $\lambda = 2.12 \mu\text{m}$ the diffraction-limited resolution of 74 mas was attained. The reconstructed visibility reveals a spherically symmetric, circumstellar dust shell (CDS) surrounding the central star. The visibility function shows that the stellar contribution to the total flux at $\lambda = 2.12 \mu\text{m}$ is less than $\sim 50\%$, indicating a rather large optical depth of the CDS. The azimuthally averaged 1-dimensional Gaussian visibility fit yields a diameter of 47 ± 3 mas ($FHWM$), which corresponds to 112 ± 13 AU for an adopted distance of $D = 2.38 \pm 0.24$ kpc. To determine the structure and the properties of the CDS of OH 104.9+2.4, radiative transfer calculations using the code DUSTY were performed to simultaneously model its visibility and the spectral energy distribution (SED). We found that both the ISO spectrum and the visibility of OH 104.9+2.4 can be well reproduced by a radiative transfer model with an effective temperature $T_{\text{eff}} = 2500 \pm 500$ K of the central source, a dust temperature $T_{\text{in}} = 1000 \pm 200$ K at the inner shell boundary $R_{\text{in}} \approx 9.1 R_{\star} = 25.4$ AU, an optical depth $\tau_{2.2 \mu\text{m}} = 6.5 \pm 0.3$, and dust grain radii ranging from $a_{\text{min}} = 0.005 \pm 0.003 \mu\text{m}$ to $a_{\text{max}} = 0.2 \pm 0.02 \mu\text{m}$ with a power law $n(a) \propto a^{-3.5}$. It was found that even minor changes in a_{max} have a major impact on both the slope and the curvature of the visibility function, while the SED shows only minor changes. Our detailed analysis demonstrates the potential of dust shell modeling constrained by both the SED and visibilities.

Key words. radiative transfer – stars: AGB and post-AGB – stars: mass-loss – stars: circumstellar matter – infrared: stars – stars: individual: OH 104.9+2.4

1. Introduction

OH 104.9+2.4 (IRAS 22177+5936, AFGL 2885, NSV 25875) is an OH/IR type II-A class star. These objects exhibit the maximum of their SED in the infrared (IR) around $6\text{--}10 \mu\text{m}$, while the $9.7 \mu\text{m}$ silicate feature is found to be in absorption. In addition, they show strong OH maser line emission at 1612 MHz/18 cm (Habing 1996) and weaker emission in SiO (43.1 GHz and 86.2 GHz), in H₂O (22.2 GHz), and in the other hyperfine OH lines of the same transition (1665/1667 MHz, 1720 MHz) (Herman & Habing 1985). OH/IR stars are long-period variables (pulsation periods between 500 and 3000 d) of variability type Me, similar to long-period Mira stars. While the majority of OH/IR stars show a bolometric amplitude of typically ~ 1 mag, a very small fraction varies irregularly with a low amplitude or does not show any detectable variability. OH/IR stars are mostly low and intermediate mass (progenitor masses $M \leq 9 M_{\odot}$), oxygen-rich single stars evolving along the upper part of the asymptotic giant branch (AGB). OH/IR stars extend the sequence of

optical Mira variables towards longer periods, larger optical depths and higher mass-loss rates (Engels et al. 1983; Lepine et al. 1995). As a consequence of their high mass loss, OH/IR stars are surrounded by massive, optically and geometrically thick circumstellar envelopes composed of gas and dust. The strong maser emission reveals non-rotating CDS (Herman & Habing 1985), which, in some cases, totally obscures the underlying star.

Observations as well as theoretical models of the structure, dynamics, and evolution of the atmosphere and CDS of AGB stars have led to a detailed picture of these objects. According to Habing (1996), OH/IR stars are characterized by the following parameters: a variation of the bolometric flux $\Delta m_{\text{bol}} > 0.7$ mag, luminosities $L > 3 \times 10^3 L_{\odot}$, effective temperatures $T_{\text{eff}} < 3000$ K, temperatures at the inner boundary of the CDS $T_{\text{in}} \approx 1000$ K, optical depths $\tau_{9.7 \mu\text{m}} \approx 10^{-2}\text{--}10^1$, the silicate feature at this wavelength always in absorption, and high mass-loss rates ($\dot{M} \approx 10^{-7}\text{--}10^{-4} M_{\odot}/\text{yr}$) at moderate outflow velocities ($v_e \approx 10 \text{ km s}^{-1}$). The AGB phase and therefore the phase of high mass loss typically lasts for some 10^5 yr. Lorenz-Martins & de Araujo (1997) find $T_{\text{eff}} \approx 1800\text{--}2400$ K,

[★] Based on data collected at the 6 m BTA telescope of the Special Astrophysical Observatory in Russia.

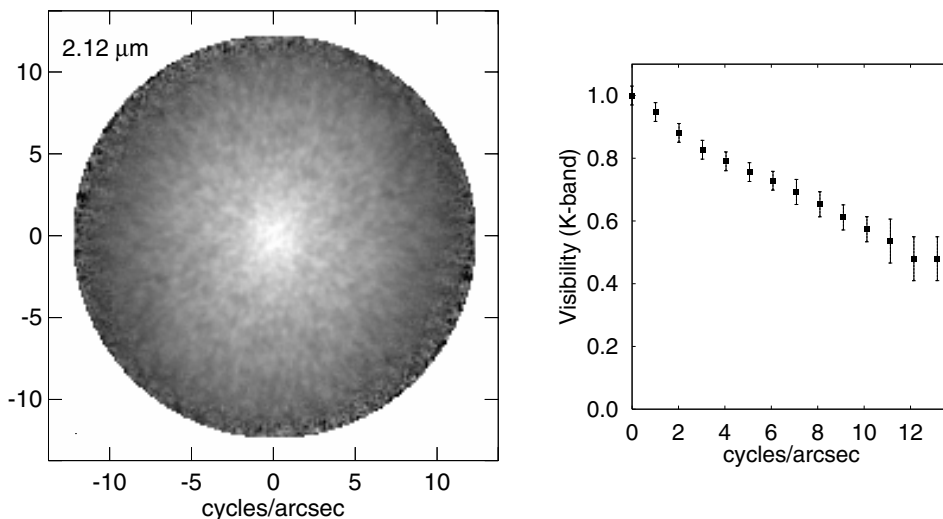


Fig. 1. Observations of OH 104.9+2.4 on September 22, 2002, with the SAO 6 m telescope. *Left:* 2-dimensional 2.12 μm visibility function of OH 104.9+2.4. *Right:* azimuthally averaged visibility of OH 104.9+2.4 in the K' band.

$T_{\text{in}} \approx 650\text{--}1200$ K, $\tau_{9.7 \mu\text{m}} \approx 7\text{--}17$, and the silicate feature typically in absorption for many OH/IR stars.

The mass loss is driven by both large-amplitude pulsations and acceleration by radiation pressure. Therefore, correlations are found between the period and the terminal outflow velocity (e.g. Heske 1990). Detailed hydrodynamical models show that, due to the passage of shocks generated by the stellar pulsation, the atmosphere is highly extended, thus enabling dust formation and the subsequent acceleration of matter (see, e.g., Höfner et al. 2003; Schirrmacher et al. 2003; Jeong et al. 2004, and references therein).

The assumption of a spherically symmetric dust shell is frequently motivated by the circularity of OH maser maps. High-spatial-resolution observations can give direct information about the extension and geometry of the CDS and therefore lead to more reliable constraints for the modeling of the circumstellar environment, supplementing the information from the SED. Measurements of the near-IR (NIR) visibility may be used to determine the radius of the onset of dust formation as well as to constrain the grain sizes (Groenewegen 1997).

OH 104.9+2.4 is a representative example of a type II-A OH/IR variable. From the variations of the 1612 MHz OH maser, a period of $P = 1216 \pm 54$ d was determined (Herman & Habing 1985), although values up to 1620 d have been found (Jones et al. 1990). The radial outflow velocity of $v_e = 15 \text{ km s}^{-1}$ measured (te Lintel Hekkert et al. 1991) is in accordance with SiO and H₂O maser observations (Engels et al. 1986). From maser phase lag measurements, an outer radius of the dust shell of $R_S = (4.37 \pm 0.42) \times 10^{16}$ cm was determined, while the absolute distance was found to be $D = 2.38 \pm 0.24$ kpc (Herman & Habing 1985). A mass-loss rate of $\dot{M} = 5.58 \times 10^5 M_{\odot}/\text{yr}$ was derived by Heske et al. (1990).

The paper is organized as follows: in Sect. 2, results of NIR speckle interferometric observations of OH 104.9+2.4 are presented. Section 3 deals with the SED reconstruction. The approach for the radiative transfer modeling (RTM), as well as the strategy of simultaneous modeling of SED and near-infrared visibility is outlined in Sect. 4.1. The method described was recently applied to other evolved stars, such as

Red Rectangle (Men'shchikov et al. 1998), AFGL 2290 (Gauger et al. 1999), IRC+10420 (Blöcker et al. 1999), NML Cyg (Blöcker et al. 2001) and CIT 3 (Hofmann et al. 2001). Sections 4.2–4.4 give details of the modeling results, and Sect. 5 closes the discussion with a summary of the results, a conclusion and an outlook. Additional results will be presented in a subsequent publication (Riechers et al. 2004).

2. Speckle interferometry observations and data reduction

The K' -band speckle interferograms of OH 104.9+2.4 were obtained with the Russian 6 m telescope of the Special Astrophysical Observatory (SAO) on September 22, 2002. The data were recorded with our HAWAII speckle camera through interference filters with a center wavelength of 2.12 μm and a bandwidth of 0.21 μm (K' band). Additional speckle interferograms were taken for three unresolved reference stars (GJ 105.5, G 77-31, and HD 22686). With a pixel size of 27 mas and a seeing of 1.9 arcsec ($1.5 \cdot FWHM$ of centered long exposure), 444+727 object frames and 690+792 frames of the reference stars were taken, each with an exposure time of 268 ms. These interferograms were used to compensate for the speckle interferometry transfer function. The visibility function of OH 104.9+2.4 was derived from the speckle interferograms using the speckle interferometry method (Labeyrie 1970). The reconstructed two-dimensional visibility at 2.12 μm and the azimuthally averaged visibility profile is shown in Fig. 1. The azimuthally averaged visibility decreases steadily to values below ~ 0.50 at the diffraction cut-off frequency (13.5 cycles/arcsec). Thus, the CDS is almost fully resolved, and the contribution of the unresolved component to the monochromatic flux at $\lambda = 2.12 \mu\text{m}$ is less than $\sim 50\%$, indicating a rather large optical depth at this wavelength. In order to give a first, rough estimate for the apparent diameter of the dust shell, the azimuthally averaged visibility was fitted with a Gaussian and a uniform disk (UD) center-to-limb variation. We obtain a Gaussian fit $FWHM$ diameter of 47 ± 3 mas, which corresponds to a diameter of 112 ± 13 AU for an adopted distance of $D = 2.38 \pm 0.24$ kpc (Herman & Habing 1985).

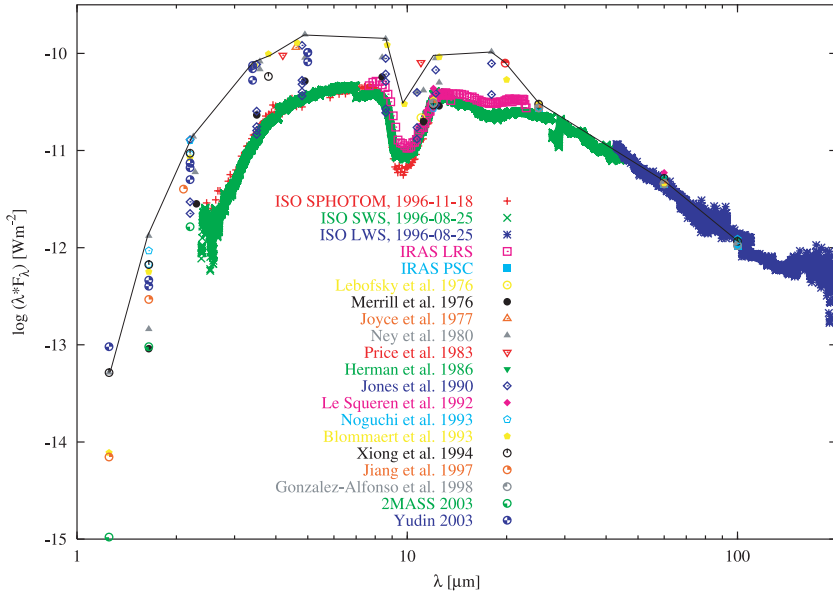


Fig. 2. SED of OH 104.9+2.4. The ISO SED appears to be taken at near-minimum pulsation phase ($\Phi_{\text{ISO}} = 0.5$). The black line depicts a maximum envelope for the SED, which was used to derive the bolometric flux at maximum phase.

Table 1. Infrared photometry of OH 104.9+2.4. The observations were carried out by Yudin (2003). All observations are given in magnitudes.

Date	Julian date	<i>J</i>	<i>H</i>	<i>K</i>	<i>L</i>	<i>M</i>
Aug. 14, 2003	2452 866.50		9.04	5.20	1.16	-0.06
Sep. 08, 2003	2452 891.42	11.53	9.19	5.32	1.24	-0.06
Dec. 10, 2003	2452 984.20			5.63	1.54	0.18

The UD diameter is found to be 73 ± 5 mas, corresponding to 173 ± 22 AU. The quality of the visibility fits with both the Gaussian model and the UD are rather poor, as the shape of the observed visibility strongly deviates from that of a Gaussian or UD visibility. From our observations, no major deviation from spherical symmetry was detected, in accordance with the analysis of OH maser maps (Welty et al. 1987). Given the accuracy and resolution of our visibility measurement, we find that the diameter ratio between major and minor axis deviates from unity by less than 8%. Therefore, we restricted the further discussion and the modeling itself to the azimuthally averaged 1-dimensional visibility and the usage of a 1D-radiative transfer code.

3. Spectral energy distribution

Photometric and spectroscopic data in the IR for OH 104.9+2.4 have been reported, for example, by Lebofsky et al. (1976), Merrill et al. (1976), Joyce et al. (1977), Ney et al. (1980), Price et al. (1983), Knacke et al. (1985), Herman et al. (1986), Cobb et al. (1987), Jones et al. (1990), Le Squeren et al. (1992), Noguchi et al. (1993), Blommaert et al. (1993), Xiong et al. (1994), Jiang et al. (1997), Gonzalez-Alfonso et al. (1998), and Cutri et al. (2003). OH 104.9+2.4 was observed by IRAS (Infrared Astronomical Satellite) in 1983 and by ISO (Infrared Space Observatory) in 1996. In Fig. 2, the SED of OH 104.9+2.4 is shown. In addition to the cited data, recent data obtained by Yudin (2003) at the Crimean Astrophysical Observatory (CAO) on August 14, 2003, September 08, 2003, and December 10, 2003, in the *J*, *H*, *K*, *L*, and *M* bands (Table 1) are shown. The reference star for these observations

was BS 8465 ($J = 0.97^m$, $H = 0.28^m$, $K = 0.11^m$, $L = 0.00^m$, $M = 0.20^m$). OH 104.9+2.4 shows strong long-term SED variations (see Fig. 2). The ISO data were most likely taken at minimum pulsation phase, as all other data points lie above the ISO spectrum. Therefore, we adopt $\Phi_{\text{ISO}} \approx 0.5$. From the ISO data, a near-minimum bolometric flux of $F_{\text{bol}}^{\text{ISO}} = 6.99 \times 10^{-11} \text{ W/m}^2$ can be derived. In order to find the bolometric flux at the phase of the SAO observations, a bolometric flux at maximum phase has to be determined first. To obtain this bolometric flux, we defined a maximum envelope representing the maximum-luminosity SED as depicted by the black line in Fig. 2, which takes into account the wavelength dependence of the pulsation amplitude, and obtain $F_{\text{bol}}^{\text{max}} = 2.30 \times 10^{-10} \text{ W/m}^2$. With *K*-band data measured by Jones et al. (1990), Noguchi et al. (1993), Cutri et al. (2003), and Yudin (2003) and a simple cosine-like pulsation model, we derived a pulsation period of $P = 1500 \pm 11$ d, applying a 4-parameter least-squares fit ($f(x) = a \cdot \cos(2\pi x/P - b) + c$), as shown in Fig. 3. We would like to point out, that this model is not physically accurate, but a suitable choice regarding the low number of data points. With this model fit, we find $\Phi_{\text{SAO}} \approx 0$. Therefore, $F_{\text{bol}}^{\text{SAO}} = 2.30 \times 10^{-10} \text{ W/m}^2$ can be assumed, corresponding to a factor of ~ 3.3 relative to the flux at Φ_{ISO} . This difference in F_{bol} has to be taken into account in the modeling process.

OH 104.9+2.4 is highly reddened by the interstellar medium (ISM) and its CDS. The interstellar reddening was taken into account by adopting the method of Savage & Mathis (1979) with $A_V = 3.1 \cdot E(B - V)$. For a distance of $D = 2.38 \pm 0.24$ kpc, we found $A_V = 4.09$. This correction was applied to all models as described by Men'shchikov et al. (2002a).

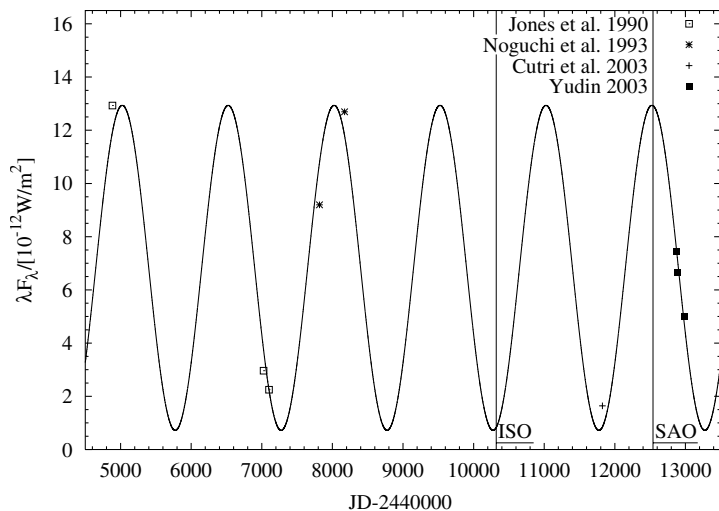


Fig. 3. Recent observations of OH 104.9+2.4 at $\lambda = 2.2 \mu\text{m}$. Measurements by Jones et al. (1990), Noguchi et al. (1993), Cutri et al. (2003) and Yudin (2003) are shown. A 4-parameter cosine function is fitted (least-squares method) to the data and provides a pulsation period of $P = 1500 \pm 11$ d. The left vertical line indicates the date of the ISO measurements and substantiates the assumption of $\Phi_{\text{ISO}} = 0.5$. The right vertical line indicates the date of the SAO measurements and allows us to derive $\Phi_{\text{SAO}} \approx 0$.

4. Dust shell models

4.1. The radiative transfer code

The radiative transfer calculations were performed using the publicly available code DUSTY (Ivezić et al. 1999). The main assumptions involved are (for single-shell models): (i) constant spherical symmetry with $\rho(r) \propto r^{-n}$; (ii) a constant dust-to-gas ratio; (iii) a constant dust opacity and size distribution; (iv) radiative equilibrium; (v) the same temperature $T_d(a, r) = T_d(r)$ for all dust grains; and (vi) isotropic scattering. With these assumptions, the only relevant property of the input radiation is its spectral shape $f_\lambda = F_\lambda/F$. The overall optical depth of the dust envelope at some reference wavelength τ_λ fixes the solution, allowing only for normalized density distributions ρ_d describing the spatial variation of the dust, and the wavelength dependence of the optical properties of the dust grains.

The DUSTY formulation of the radiative transfer problem for a dusty envelope is very suitable for modeling of IR observations, since it minimizes the number of independent model input parameters. The only parameters that have to be specified are (i) the spectral shape of the central source of radiation f_λ (i.e. the variation of the monochromatic flux with wavelength); (ii) the absorption/emission and scattering efficiencies of the grains (i.e. the chemical composition and the grain-size distribution); (iii) the normalized density distribution of the dust $\rho(r)/\rho_{\text{in}}$; (iv) the relative thickness of the dust shell (i.e. the ratio of outer to inner dust shell radius, $r_{\text{out}}/r_{\text{in}}$); (v) the dust temperature T_{in} at the inner boundary r_{in} ; and (vi) the overall optical depth at a reference wavelength τ_λ . For a given set of input parameters, DUSTY iteratively determines the radiation field and the dust temperature distribution (generalized output quantities) by solving the equation of radiative transfer.

4.2. Previous modeling of OH 104.9+2.4

There are two previous studies which deal with dust shell modeling of OH 104.9+2.4. The first dust shell models were reported by Ivezić et al. (1995) using a previous version of the DUSTY code. It was mainly based on IRAS data. The authors found $F_{\text{bol}} = 7.6 \times 10^{-11} \text{ W/m}^2$, $L = 1.19 \times 10^4 L_\odot$

for $D = 2.30$ kpc, $v_e = 15.1 \text{ km s}^{-1}$, $\tau_{2.2 \mu\text{m}} = 1.12$, and $\dot{M} = 3.87 \times 10^{-5} M_\odot/\text{yr}$.

A recent two-component dust shell model was reported by Suh (2002), using only the ISO SWS/LWS spectra as observational constraints. The author introduced a combined envelope/disk model to improve his fit to the observational data. The reference optical depth for his best-fitting model was $\tau_{10 \mu\text{m}} = 10.0$. To date, there has not been any modeling of OH 104.9+2.4 that uses observational constraints from both the SED and visibility measurements.

4.3. The best-fitting model

For the analysis of OH 104.9+2.4 based on the radiative transfer modeling, $\sim 10^6$ models (discussed in Sect. 4.4) were calculated. To simultaneously fit the SED and visibility data (i.e. with identical model parameters), F_{bol} had to be adjusted for the epoch of the visibility measurements, since the ISO spectrum and our visibility data were taken at different pulsation phases of OH 104.9+2.4 (see Fig. 3). Therefore, the best-fitting model (Figs. 4 and 5) consists of an SED model assuming the 1996 ISO flux and a visibility model assuming the 2002 SAO flux. The results are all summarized in Table 2.

4.3.1. SED fit

The final model that fits the ISO SED data of OH 104.9+2.4 best is presented in Fig. 4 (left panel). The black-body (BB) effective temperature of the central source of radiation is $T_{\text{eff}} = 2500$ K. In addition, $T_{\text{in}} = 1000$ K, $\rho(r)/\rho_{\text{in}} \propto r^{-2.0}$ and $r_{\text{out}}/r_{\text{in}} = 10^5$. Assuming the overall influence of the dust formation zone on the SED to be rather small, a standard $n(a) \propto a^{-3.5}$ grain-size distribution (GSD) function (Mathis et al. 1977, hereafter MRN) was chosen, with a ranging between $a_{\text{min}} = 0.005 \mu\text{m}$ and $a_{\text{max}} = 0.2 \mu\text{m}$. A dust composition with 95% of the optical constants for warm silicates from Ossenkopf et al. (1992, hereafter OHM) and 5% astronomical silicates from Draine & Lee (1984, hereafter DL) was found to give the best results. The OHM warm, oxygen-deficient silicates are based on observational determinations of the

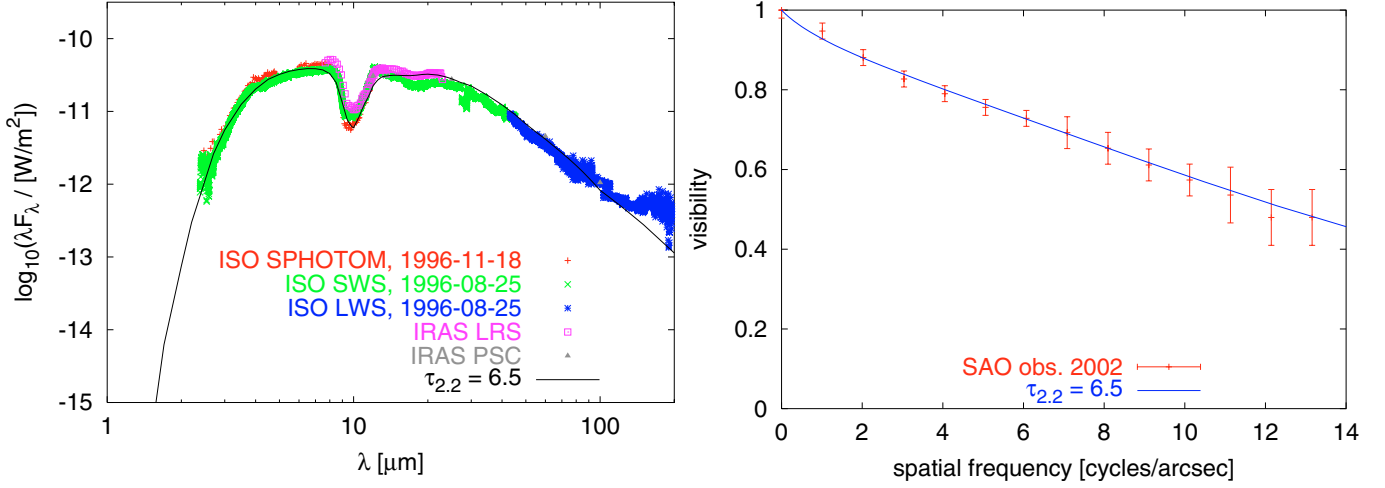


Fig. 4. SED (left) and visibility (right) of OH 104.9+2.4 for our best-fitting model. As described in the text, the bolometric flux used for the SED is a factor of 3.3 lower than the one used for the SED, in order to take into account the different epochs of the ISO and SAO observations.

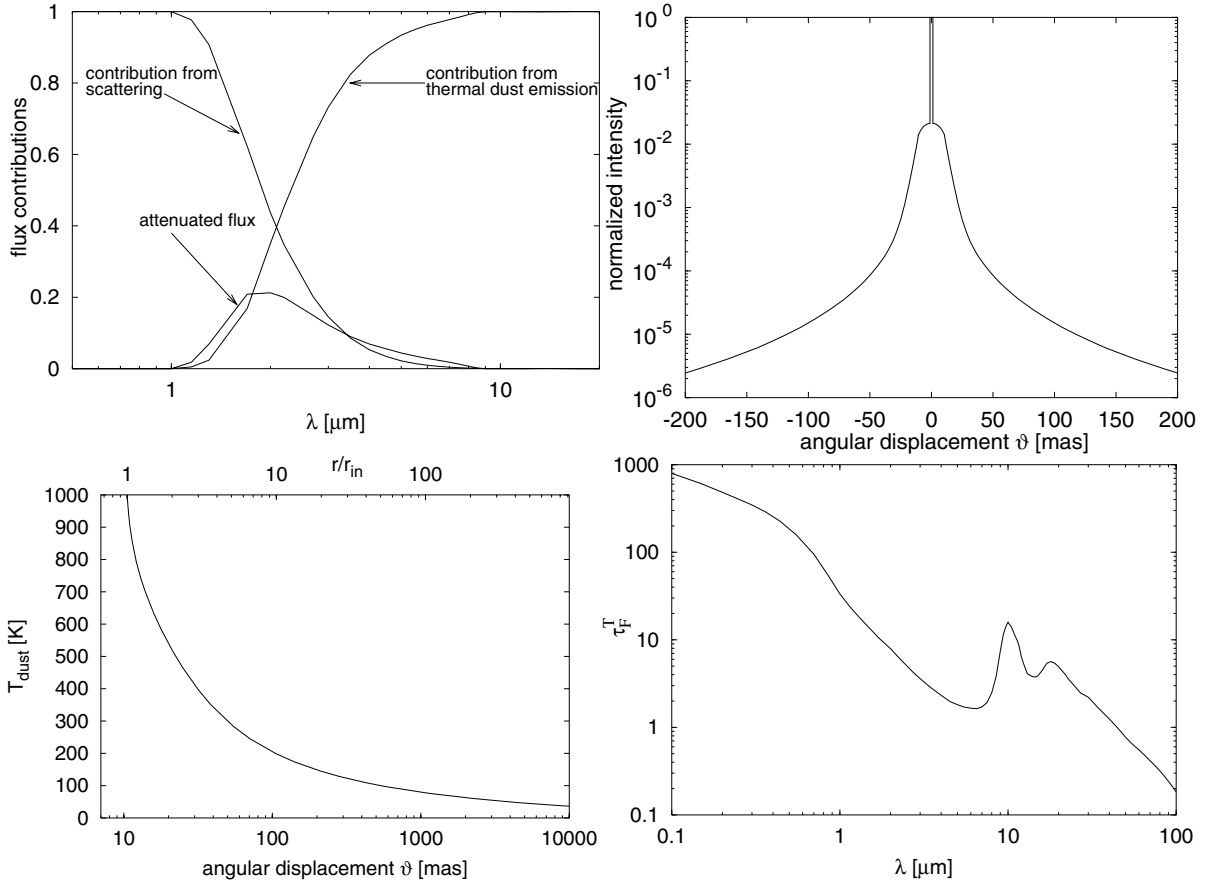


Fig. 5. Modeling results of OH 104.9+2.4 for our best-fitting model (see Table 2). *Top left:* fractional contributions to the total flux. The contribution from direct stellar light is small in comparison to the contribution of the processes in the CDS. *Top right:* the normalized intensity profile at $2.13 \mu\text{m}$. The sharp central peak corresponds to the central source of radiation. *Bottom left:* dust temperature as a function of angular distance (lower axis) and of the radius in units of the inner dust shell radius (upper axis). The point where $T_{\text{dust}} = 1000 \text{ K}$ indicates the inner radius of the dust shell ($r/r_{\text{in}} = 1$). *Bottom right:* wavelength dependence of the total optical depth.

opacities of circumstellar silicates as well as laboratory data and also take into account the effects of inclusions (amorphous and crystalline substructures as well as other materials)

on the complex refractive index, especially at $\lambda = 8 \mu\text{m}$. The reference optical depth in our best-fitting model is $\tau_{2.2 \mu\text{m}} = 6.5$, corresponding to $\tau_{9.7 \mu\text{m}} = 14.0$ for this model at the

Table 2. The derived physical parameters of OH 104.9+2.4 as provided by the best-fitting model.

Parameter	Value	Varied range	Impact on SED/Visibility
Effective temperature (black-body)	$T_{\text{eff}} = 2500 \pm 500$ K	1500 ... 5000 K	Very weak/Weak
Temperature at inner CDS boundary	$T_{\text{in}} = 1000 \pm 200$ K	500 ... 3000 K	Moderate/Moderate
Density profile within the CDS	$\rho(r) \propto r^{-n}$ with $n = 2.0 \pm 0.1$	-1 ... 4*	Moderate/Weak
Relative CDS thickness	$\frac{r_{\text{out}}}{r_{\text{in}}} = 10^p$ with $p = 5_{-2}^{+\infty}$	1 ... 7	Very weak/Very weak ($p \geq 3$), Moderate/Weak ($p \leq 3$)
Dust grain distribution function	MRN, $n(a) \propto a^{-q}$ with $q = 3.5$	2 ... 5**	Moderate/Strong
Minimum grain size	$a_{\text{min}} = 0.005 \pm 0.003$ μm	0.0005 ... 0.5 μm	Very weak/Moderate
Maximum grain size	$a_{\text{max}} = 0.2 \pm 0.02$ μm	0.05 ... 500 μm	Weak/Very strong
Dust types	95% OHM warm silicates 5% DL astronomical silicates		Very strong/Weak
Optical depth	$\tau_{0.55 \mu\text{m}} = 158 \pm 7$ $\tau_{2.2 \mu\text{m}} = 6.5 \pm 0.3$ $\tau_{9.7 \mu\text{m}} = 14.0 \pm 0.6$	0.5 ... 100	Moderate/Strong
Radius	$R_{\star} \simeq 600 R_{\odot} = 2.79$ AU		
Radius of inner CDS boundary	$R_{\text{in}} = 9.1 R_{\star} = 25.4$ AU		
Radius of $I = 10^{-10} I_{\text{max}}$	$R_{\text{out}}^{-10} = 5 \times 10^3 R_{\star} = 1.4 \times 10^4$ AU		
Outer radius of the model	$R_{\text{out}} = 9.1 \times 10^5 R_{\star} = 2.5 \times 10^6$ AU		
Mass-loss rate	$\dot{M} = 2.18 \times 10^{-5} M_{\odot}/\text{yr}$		

* Parameter variation includes broken power laws, superwind models and models with radiatively driven winds.

** Parameter variation includes test of alternative grain size distributions (see text).

prominent silicate absorption feature. The observational value of $F_{\text{bol}} = 6.99 \times 10^{-11}$ W/m² from the ISO data can be reproduced well by our model.

From the shortest wavelength at $\lambda = 2.38$ μm up to $\lambda = 196$ μm , the model provides a good fit to the observations. The location, shape, and strength of the silicate feature at $\lambda = 9.7$ μm caused by SiO stretching vibrations is fairly well reproduced by the given composition. In the $\lambda \simeq 18$ μm region, where SiO₂ bending vibrations dominate the spectrum, there is a noticeable deviation from the observational data. Above $\lambda \simeq 100$ μm , the model falls off too steeply to fit the data. On the one hand, this may be caused by deteriorating data quality towards the long wavelengths. On the other hand, the discrepancy at longer wavelengths may be due to the fact that DUSTY uses a GSD as input but internally averages dust properties over the entire size distribution.

4.3.2. Visibility fit

From Fig. 2 it is obvious that the ISO SED and the SAO visibility data were taken at different pulsation phases. While the ISO observations were made at near-minimum phase, the SAO data were taken at near-maximum phase. Therefore, it is quite natural that the two constraints cannot be fulfilled by one model alone with the same F_{bol} . A factor of ~ 3.3 in terms of the flux at ISO phase has to be introduced to the visibility model if it is to be comparable to the SED model, as outlined in Sect. 3. If we combine the best-fitting SED model with $F_{\text{bol}} = 6.99 \times 10^{-11}$ W/m² from the previous subsection with a corresponding visibility model with $F_{\text{bol}} = 2.30 \times 10^{-10}$ W/m², we obtain a very good simultaneous model for the SED and the visibility of OH 104.9+2.4, as shown in Fig. 4. However, it should be stated that the physical conclusions that can be made

based on this simultaneity itself are limited because of the simplifications involved in the phase alignment and the simplicity of the pulsation model itself (only flux scaling, assumption of time-independent T_{eff} and R_{\star}). Therefore, all further derived quantities are given for the phase of the ISO measurements unless explicitly stated otherwise.

4.3.3. Further model results

The top left panel of Fig. 5 shows the fractional flux contributions of the emerging stellar radiation, the scattered radiation, and thermal dust emission as a function of wavelength, for our best-fitting model. At 2.2 μm , the flux is dominated by thermal dust emission (45%) and scattering (35%). Direct stellar light (attenuated flux) contributes only 20% at this wavelength. Thus, scattering contributes nearly to the same extent to the radiation of the CDS in the *K* band as thermal dust emission. At shorter wavelengths scattering dominates, while dust emission is the major flux contribution at wavelengths longer than 3 μm . The attenuated flux from the central source plays a minor role at all wavelengths under consideration (0.01 μm –0.03 m) due to nearly total obscuration.

The top right panel of Fig. 5 shows the normalized intensity distribution at 2.13 μm as a function of angular distance. The barely resolved central peak corresponds to the central star. At the given optical depth of $\tau_{2.2 \mu\text{m}} = 6.5$, there is no evidence for limb-brightening effects at the inner boundary, due to the extreme optical thickness of the CDS. If we define an outer radius of the dust shell R_{out}^{-10} at the point where the intensity at 2.13 μm is $I_{\text{out}}^{-10} = 10^{-10} \cdot I_{\text{max}}$, this point is found at approximately $\vartheta_{\text{out}}^{-10} = 5.8$ arcsec.

The bottom left panel of Fig. 5 shows a plot of the dust temperature as a function of angular distance and in units of the

inner radius of the dust shell, respectively. The inner CDS radius r_{in} can be derived directly from the radial profile, as it is the point at which the dust reaches $T_{\text{in}} = 1000$ K. It corresponds to an angular radius of $\vartheta_{\text{in}} = 10.5$ mas.

The bottom right panel of Fig. 5 shows the total optical depth as a function of wavelength. As expected, local maxima of τ_{λ} are found for the silicate absorption features at $9.7 \mu\text{m}$ (SiO stretching vibrations) and $18 \mu\text{m}$ (SiO₂ bending vibrations).

The stellar radius obtained for the best-fitting model is $\vartheta_{\star} = 1.16$ mas. This corresponds to $R_{\star} \simeq 600 R_{\odot}$ or 2.79 AU for the adopted distance of $D = 2.38 \pm 0.24$ kpc. Therefore, the inner radius of the CDS is $R_{\text{in}} = 9.1 R_{\star} = 25.4$ AU. This value is rather high and results from the very high optical depth leading to high dust temperatures, so that closer to the central star the dust grains evaporate (see Men'shchikov et al. 2002b). The outer radius of the CDS as defined above is at $R_{\text{out}}^{-10} = 5 \times 10^3 R_{\star} = 1.4 \times 10^4$ AU. From the definition of R_{out}^{-10} , it follows that $R_{\text{out}}^{-10}/R_{\text{in}} = 550$, and since $I_{\text{out}}(R_{\text{out}}^{-10}) = 10^{-10} I_{\text{max}}$, only a fraction of the order of 10^{-7} of the total flux comes from a region with $r \geq R_{\text{out}}^{-10}$. This explains why models with $r_{\text{out}}/r_{\text{in}} > 10^3$ do not show much of a change with rising $r_{\text{out}}/r_{\text{in}}$. The value obtained under this assumption is of the same order as that found by Herman & Habing (1985) and therefore seems to give a reliable lower limit for the outer diameter of the dust shell. They derived $R_{\text{S}} = 4.37 \pm 0.42 \times 10^{16}$ cm = $2.92 \pm 0.28 \times 10^3$ AU = $6.3 \times 10^5 R_{\odot} \simeq 10^3 R_{\star}$. However, the modeling as well as the observations are both fully allegeable with a dust shell that extends from R_{in} to infinity.

From the observations, the total luminosity can be derived according to

$$\frac{F_{\text{bol}}}{[10^{-10} \text{ W/m}^2]} = 3.21 \cdot \frac{L}{[10^4 L_{\odot}]} \cdot \left(\frac{D}{[\text{kpc}]} \right)^{-2}. \quad (1)$$

This leads to a luminosity of $L_{\text{obs}} = (1.23 \pm 0.12) \times 10^4 L_{\odot}$ for the bolometric flux at Φ_{ISO} which is in very good agreement with the value $L_{\text{mod}} = 1.262 \times 10^4 L_{\odot}$ obtained from our best-fitting model using the Stefan-Boltzmann law.

According to the mass-luminosity relation by Ivezić et al. (1995), this corresponds to a central star mass of $M \simeq 1 M_{\odot}$, which is in line with predictions from stellar evolution theory for stars in this evolutionary stage.

Following Ivezić et al. (1995), the mass-loss rate \dot{M} can be derived from

$$\dot{M} v_e = \tau_{\text{F}} \cdot \frac{L}{c} \cdot \left(1 - \frac{1}{\Gamma} \right), \quad (2)$$

where

$$\Gamma = \frac{F_{\text{rad}}}{F_{\text{grav}}}$$

is the ratio of radiation pressure F_{rad} and gravitational force F_{grav} per unit volume in the envelope. With $\tau_{\text{F}} = 3.2$, $\Gamma = 1.7 \cdot L$ from our best-fitting model and the adopted outflow velocity $v_e = 15 \text{ km s}^{-1}$ from te Lintel Hekkert et al. (1991), $\dot{M} = 2.18 \times 10^{-5} M_{\odot}/\text{yr}$ is obtained.

4.4. Parameter variations

In this section, we discuss the impact of several input parameters on the process of radiative transfer modeling. The best-fitting model (see Sect. 4.3) is used as a basis for the discussion, and the effect of the variations of the parameters in question is outlined. The discussion is divided into subsections, in which the change of each parameter is discussed separately. To maintain the presentation as concise as possible, the variations for minor parameters like a_{min} and the discussion of more complex models (e.g. broken power law density distributions, multiple discrete dust shells), that did not deliver better fits than the models with less assumptions are omitted.

4.4.1. Dust types

One of the most important quantities that have to be fixed in the modeling process is the chemical composition of the dust itself. Here, four different dust types are under discussion, namely (i) that of the best-fitting model, which is mainly the warm, oxygen-deficient silicates from Ossenkopf et al. (1992); (ii) the type given by the same authors as cold, oxygen-rich silicates; (iii) the astronomical silicates by Draine & Lee (1984), which are also included as a small fraction in the dust type of our best-fitting model (5%); and finally (iv) the α -SiC grains tabulated by Pegourie (1988). The results of radiative transfer modeling obtained for these different grain types, with all other parameters fixed to the value of the best-fitting model, are presented in Fig. 6a. The models with OHM cold silicates give a slightly worse fit to the data than the models with the warm silicates. In general, the DL silicates provide good model fits, though these are not as good as those provided by the OHM warm silicates. The small fraction of DL silicates was added to the dust composition of the best-fitting model to correctly reproduce the depth of the $9.7 \mu\text{m}$ silicate feature. With all other model parameters fixed to the values of the best-fitting model (see Sect. 4.3), we need $\tau_{2.2 \mu\text{m}} = 2.0$ to fit the SED for DL silicates, implying excessive flux at the shorter wavelengths, but $\tau_{2.2 \mu\text{m}} = 5.0$ for a good visibility fit. The Pegourie SiC composition seems to be unsuitable, as no good overall fit to SED and visibility can be found. It is possible to reproduce the depth of the silicate feature with an optical depth of $\tau_{2.2 \mu\text{m}} = 18.0$, but with a great vertical offset (which clearly is due to the fact that SiC has vibrational modes different from SiO), and the visibility can be fitted with $\tau_{2.2 \mu\text{m}} = 6.0$.

4.4.2. Effective temperatures

Figure 6b shows the variations of the model SED and visibility with the effective temperature of the central star. For a fixed optical depth, a higher value for T_{eff} leads to lower flux at both shorter wavelengths and at the $9.7 \mu\text{m}$ silicate feature, and higher flux at the long-wavelength tail. The changes are qualitatively similar to those introduced by a variation of T_{in} (see next subsection) but much weaker due to the rather large $\tau_{2.2 \mu\text{m}}$ considered here. The main reason for the changes described is the shift of the peak-intensity wavelength of the stellar black-body spectrum which induces changes in the radial temperature

profile of the dust: the dust temperature falls off more steeply for higher effective temperatures. The effect on the visibility is rather small in slope and curvature and can be compensated by a small change in $\tau_{2.2\ \mu\text{m}}$, as shown for $T_{\text{eff}} = 2000\ \text{K}$ in Fig. 6b. The visibilities for the model with $\tau_{2.2\ \mu\text{m}} = 6.5$ and $T_{\text{eff}} = 2500\ \text{K}$ and the one with $\tau_{2.2\ \mu\text{m}} = 7.0$ and $T_{\text{eff}} = 2000\ \text{K}$ are almost identical.

4.4.3. Temperatures at the inner boundary

Figure 6c shows the model variations with changing temperature T_{in} at the inner dust shell boundary. For $\tau_{2.2\ \mu\text{m}}$ as high as in our favored model, decreasing T_{in} lowers the flux at shorter wavelengths, increases the depth of the $9.7\ \mu\text{m}$ silicate feature, and raises the flux at the long-wavelength tail. This behavior is similar to the changes produced by increasing $\tau_{2.2\ \mu\text{m}}$. Therefore, changes in the SED due to a variation of T_{in} can, in principle, be compensated by a corresponding variation of $\tau_{2.2\ \mu\text{m}}$, as illustrated in Fig. 6c for $T_{\text{in}} = 850\ \text{K}$ and $T_{\text{in}} = 1200\ \text{K}$. On the other hand, the depth of the silicate feature constrains the choice of the optical depth. For the visibility function, lowering T_{in} leads to a steeper decline at low spatial frequencies and a stronger curvature, and therefore a shallower fall-off at high spatial frequencies. With an adjusted optical depth (as shown for $T_{\text{in}} = 850\ \text{K}$ and $T_{\text{in}} = 1200\ \text{K}$), the steepness rises, and the curvature decreases with increasing T_{in} . Finally, it can be concluded that even if models of similar quality to the best-fitting model can be found with different T_{in} , the value of T_{in} will be close to $1000\ \text{K}$.

4.4.4. Reference optical depths

The optical depth τ is the main parameter in this study. The variation of this quantity has a strong impact on both the SED and the visibility (see Fig. 6d). For the SED, the flux at short wavelengths for low optical depths is relatively high, whereas at long wavelengths it is relatively low. In addition, the SiO feature at $9.7\ \mu\text{m}$ is found in emission at the lowest values for $\tau_{2.2\ \mu\text{m}}$. For high optical depths, more flux is reprocessed to long wavelengths as a result of the stronger reddening effects. The most important constraint for this parameter is the depth of the $9.7\ \mu\text{m}$ absorption feature, which is too deep for very high optical depths. The visibility mostly keeps its curvature, but steepens for higher optical depths due to the stronger obscuration of the central source. The steepening shows a roughly linear dependence on the optical depth in the domain under consideration. The best value for a simultaneous SED and visibility model is found to be $\tau_{2.2\ \mu\text{m}} = 6.5$.

4.4.5. Grain sizes

In Fig. 7a, models assuming an MRN grain-size distribution with different maximum grain size a_{max} are shown. All other parameters are fixed to the values of the best-fitting model presented in Sect. 4.3. Concerning the SED, a_{max} provides a strong constraint for the scattering and absorption efficiency. The averaged (over the size distribution) scattering efficiency

per unit volume of the grains $Q_{\text{sca}}/\hat{V} \propto a^3$ steeply declines with increasing wavelength, and can be neglected above a certain wavelength, depending on a_{max} (for an example, we refer to Fig. 5, top left panel of the best-fitting model). The size-averaged absorption efficiency depends on the grain size only at short wavelengths and becomes independent of a_{max} when $\lambda \gg a$ (see Fig. 8). Therefore, the fluxes observed at the shortest wavelengths place an upper limit on the maximum grain size. The depth of the $9.7\ \mu\text{m}$ silicate absorption feature itself leads to the prediction that $a_{\text{max}} \leq 0.50\ \mu\text{m}$ for the current configuration. In the long wavelength regime ($\lambda \geq 100\ \mu\text{m}$), it is possible to find a model that fits better than the best-fitting model, but the improvement of the fit quality is relatively small. The slightly better fit might be due to a fixed F_{bol} in combination with the fact that the models in question become optically thin at short wavelengths (Fig. 8), since the large grains engross large fractions of the dust mass. In this case, a large fraction of F_{bol} is emitted at short wavelengths, resulting in lower flux at long wavelengths. In addition, the problems mentioned in Sect. 4.3.1 may play a role.

The K' -band visibility is very sensitive against scattering and thus depends strongly on the assumed grain sizes. Increasing a_{max} has a similar effect to increasing the optical depth and results in a stronger decline of the visibility function. As an MRN-like distribution declines very steeply towards larger grain sizes, most of the particles in the model remain small when a_{max} is increased. But, due to the strong dependence of the scattering and absorption properties on the grain sizes at $2.12\ \mu\text{m}$, the impact of these few extra large grains on the visibility is comparable to that of the large bulk of small grains (Krüger & Sedlmayr 1997). The curvature of the visibility changes its sign somewhere around $a_{\text{max}} \leq 0.20\ \mu\text{m}$. This behavior reflects the change of the spatial intensity distribution. At large radial offsets b from the central star, $I(b) \propto b^{-3}$ holds, since the optical depth along the line of sight becomes small (Jura & Jacoby 1986).

Regarding the wavelength dependence of the total optical depth, the choice of a_{max} is only of minor importance beyond a certain range of values (see Fig. 8). For $a_{\text{max}} \leq 1\ \mu\text{m}$ and wavelengths larger than $5\ \mu\text{m}$, the impact of the grain size is limited. The shape of the function is almost the same, and the offset can be fixed by adjusting the optical depth of the models. If the grains become too large and too few, the function approximately converges towards a power law, since the characteristics of the grains then play a minor role.

4.4.6. Grain-size distributions

Instead of the standard MRN grain-size distribution, several other GSD functions can be adopted for the dust under examination. In this study, variations of the standard MRN function have been tested.

Apart from the MRN distribution, the distribution from Kim et al. (1994, hereafter KMH) is frequently used. It assumes $n(a) \propto a^{-q} \cdot e^{-a/a_0}$, with $q = 3.5$, for $a \geq a_{\text{min}}$, where a_0 has to be fixed for the exponential falloff, which replaces the sharp upper cutoff of the MRN distribution. The value chosen here

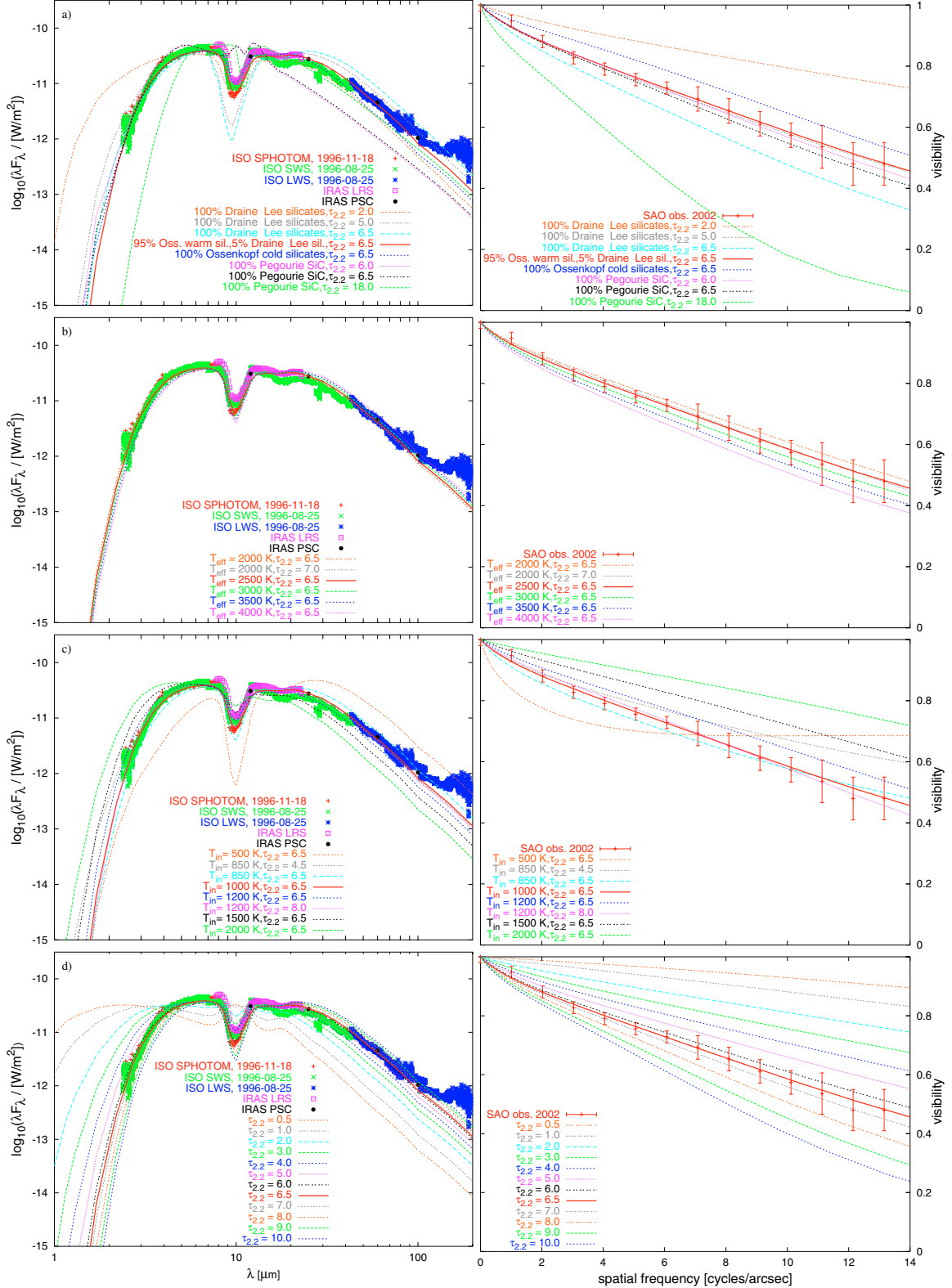


Fig. 6. SED (*left*) and K -band visibility (*right*) of OH 104.9+2.4 for the best-fitting model (thick solid line, 95% OHM warm silicates, 5% DL silicates) and the impact of several parameter variations. **a)** Variation of the dust composition. Apart from the best-fitting model models with other dust types and values of $\tau_{2.2 \mu\text{m}}$ (see labels) are shown. All other model parameters are fixed to the values of the best-fitting model. The models for DL silicates with $\tau_{2.2 \mu\text{m}} = 2.0$ and $\tau_{2.2 \mu\text{m}} = 5.0$ are given as examples for models that fit the SED and visibility with this specific dust composition. The same comparison is shown for the Pegourie (1988) SiC grains with $\tau_{2.2 \mu\text{m}} = 6.0$ and $\tau_{2.2 \mu\text{m}} = 18.0$, respectively. **b)** Variation of T_{eff} . The best-fitting model is the one with $T_{\text{eff}} = 2500$ K. For comparison, a model with $T_{\text{eff}} = 2000$ K and $\tau_{2.2 \mu\text{m}} = 7.0$ is shown, to illustrate that changing the optical depth can make up for the variations caused by T_{eff} (see text for further details). **c)** Variation of T_{in} . The best-fitting model is labeled with $T_{\text{in}} = 1000$ K. For comparison, models with $T_{\text{eff}} = 850$ K and $\tau_{2.2 \mu\text{m}} = 4.5$ as well as $T_{\text{eff}} = 1200$ K and $\tau_{2.2 \mu\text{m}} = 8.0$ are shown, to illustrate that a change of the optical depth can also make up for the variations caused by T_{in} . **d)** Variation of $\tau_{2.2 \mu\text{m}}$. The best-fitting model is labeled with $\tau_{2.2 \mu\text{m}} = 6.5$.

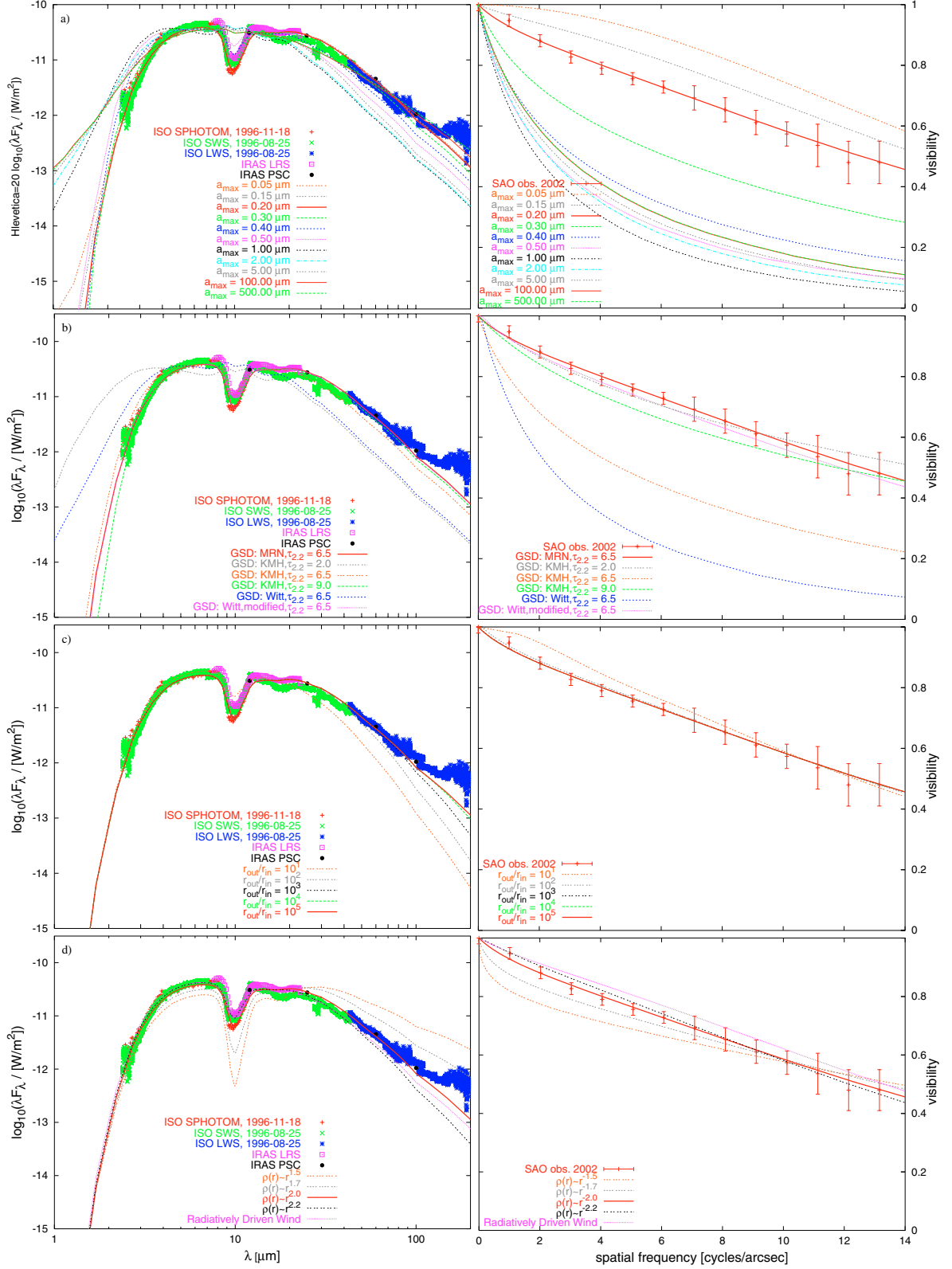


Fig. 7. SED (left) and K-band visibility (right) of OH 104.9+2.4 for the best-fitting model (thick solid line, 95% OHM warm silicates, 5% DL silicates) and the impact of several parameter variations. **a)** Variation of the maximum grain size a_{\max} . The best-fitting model is the one with $a_{\max} = 0.20 \mu\text{m}$. **b)** Variation of the grain size distribution. The best-fitting model is the one with the MRN distribution. For comparison, models with the KMH distribution and $\tau_{2.2 \mu\text{m}} = 2.0$ and $\tau_{2.2 \mu\text{m}} = 9.0$ are plotted as examples of good visibility and SED fits, respectively. **c)** Variation of the dust shell thickness. The best-fitting model is the one with $r_{\text{out}}/r_{\text{in}} = 10^5$. **d)** Variation of the slope of the radial density distribution. The best-fitting model is the one with $\rho(r) \propto r^{-2.0}$. In addition to the $\rho \propto r^{-n}$ distributions a distribution based on a radiatively driven wind model is shown (see text for details).

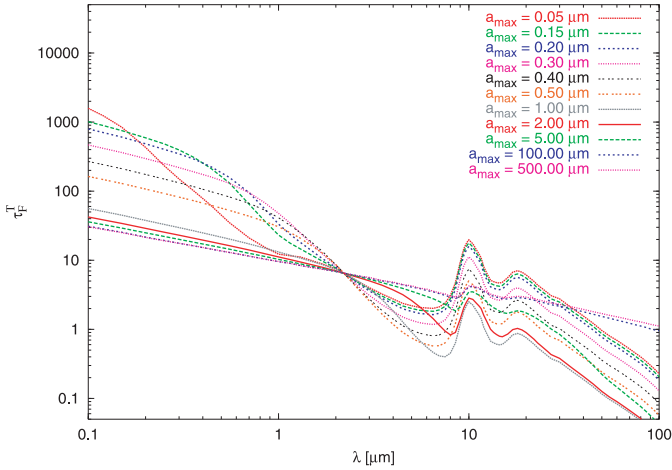


Fig. 8. Total optical depth spectrum for different maximum grain sizes (see labels).

is $a_0 = 0.17 \mu\text{m}$, which should lead to a distribution comparable to the standard MRN. The results are shown in Fig. 7b. For $\tau_{2.2 \mu\text{m}} = 6.5$, the fit is not good. For a good SED fit, $\tau_{2.2 \mu\text{m}} = 9.0$ is needed. However, we need $\tau_{2.2 \mu\text{m}} = 2.0$ for a good visibility fit. Therefore, models with a KMH grain-size distribution provide a good fit of either the SED or the visibility, but not both simultaneously.

In addition to KMH we implemented in the DUSTY code the GSD from Witt et al. (2001). Here, the MRN function remains unchanged, but a certain break point a_{break} is introduced, where the slope of the exponential decline q changes. We first used the original values $q_1 = 3.5$, $q_2 = 4.0$, $a_{\text{min}} = 0.005 \mu\text{m}$, $a_{\text{break}} = 0.5 \mu\text{m}$ and $a_{\text{max}} = 2.0 \mu\text{m}$ given by Witt et al. (2001). Obviously, results obtained with this parameter set are not directly comparable to the best-fitting model, due to different grain sizes. With $a_{\text{break}} = 0.15 \mu\text{m}$ and $a_{\text{max}} = 0.22 \mu\text{m}$, an SED fit of comparable quality to our best-fitting model is obtained, while the visibility fit is worse at intermediate spatial frequencies. Since reasonable improvements all converge towards the parameters of our best-fitting model, our assumption about the MRN GSD is justified.

4.4.7. Dust-shell thickness

In Fig. 7c different relative dust-shell thicknesses are examined. Except for the model with $\frac{r_{\text{out}}}{r_{\text{in}}} = 10$, the SED fits are almost the same up to $\lambda \approx 30 \mu\text{m}$, while the model visibility remains essentially unchanged. Taking into account the poor visibility fit, dust shells with $\frac{r_{\text{out}}}{r_{\text{in}}} \ll 10^2$ can be ruled out. Above $30 \mu\text{m}$, the SED falls off more shallowly for rising geometrical thickness, providing a better fit to the observational data. The additional cold dust introduced by the larger outer boundary increases the far infrared flux but does not affect the SED at shorter wavelengths. The only difference between the models $\frac{r_{\text{out}}}{r_{\text{in}}} = 10^4$ and $\frac{r_{\text{out}}}{r_{\text{in}}} = 10^5$ is a small deviation for $\lambda \gtrsim 120 \mu\text{m}$. Thus, from our analysis the model with $\frac{r_{\text{out}}}{r_{\text{in}}} = 10^5$ is slightly favored, whereas the relative dust-shell thickness turned out to be a non-crucial parameter in the modeling process (see also discussion above about R_{out}^{-10}).

4.4.8. Density distributions

So far, it was assumed that $\rho \propto r^{-2}$ holds within the dust shell. Assuming the outflow velocity v_e is the same as for the standard model and constant within the CDS and a constant dust-to-gas ratio, any density slope shallower/steeper than $\rho \propto r^{-2}$ means that the stellar mass-loss rate \dot{M} is non-stationary and decreases/increases with time. Figure 7d shows the result of variations in the density distribution. Since the overall agreement between observations and models worsens for $\rho \propto r^{-x}$ with $x \neq 2$, our standard density profile is justified.

For AGB stars, the envelope expansion is driven by radiation pressure on the dust grains. Therefore, a simple dust density profile $\rho(r) \propto r^{-x}$ may not be the most realistic one. If the variation of the flux-averaged opacity with radial distance as well as the grain drift is negligible, an analytic solution for the problem of a radiatively driven wind can be found (Ivezić et al. 1999) which might be more appropriate for modeling cool evolved stars such as OH 104.9+2.4. In Fig. 7d such a model is shown, whose other parameters are identical to those of our best-fitting model. The SED fit agrees with the observations at most of the wavelengths discussed. Only for short wavelengths ($\lambda < 3 \mu\text{m}$) and long wavelengths ($\lambda > 80 \mu\text{m}$) is there a noticeable deviation from the observational data. Unfortunately, no better model fit of the long wavelength regime could be obtained compared to our best-fitting model without a radiatively driven wind. In terms of the visibility, some models provide fits of comparable quality to our best-fitting model shown in Fig. 7d or even slightly better ones (with a worse SED fit). After all, both modeling approaches provide models of similar quality with otherwise identical parameters, while our best-fitting model is still slightly favoured.

5. Summary and conclusions

We present diffraction-limited $2.12 \mu\text{m}$ speckle interferometric observations of the circumstellar dust shell around the highly obscured type II-A OH/IR star OH 104.9+2.4. The resolution achieved with the SAO 6 m telescope is 74 mas, which is sufficient to fully resolve the CDS at this wavelength. From an azimuthally averaged 1-dimensional Gaussian fit of the visibility function, the diameter was determined to be $47 \pm 3 \text{ mas}$ (*FWHM*), which corresponds to a diameter of $112 \pm 13 \text{ AU}$ for an adopted distance of $D = 2.38 \pm 0.24 \text{ kpc}$. The reconstructed 2-dimensional visibility shows no major deviation from spherical symmetry.

In order to investigate the structure and the properties of the CDS, we performed 1-dimensional radiative transfer calculations to model *simultaneously* the spectral energy distribution (ISO SWS/LWS spectrum), as well as the $2.12 \mu\text{m}$ visibility function from our observations. The obtained dust shell properties correspond to a standard single-shell model (uniform outflow). Multiple component models do not match the observations better as the simple uniform outflow models, while they are certainly not excluded with the remaining uncertainties. Among the $\sim 10^6$ models calculated, the ISO SED, which appears to correspond to the minimum pulsation phase of OH 104.9+2.4, was best reproduced by a model where the

inner rim of the dust shell (i.e. the dust condensation zone) has a dust temperature of $T_{\text{in}} = 1000$ K and an angular diameter of 10.5 mas corresponding to $9.1 R_{\star}$ (Fig. 5, bottom left panel). At $2.12 \mu\text{m}$, this zone is not limb-brightened, since the model is optically thick ($\tau_{2.2 \mu\text{m}} = 6.5$).

During the entire model grid calculations, the validity of the parameters given above as well as of other parameters such as dust temperatures, grain sizes, and effective temperatures was comprehensively investigated. The grain-size distribution was found to agree with a standard MRN distribution function, $n(a) \propto a^{-3.5}$, with a ranging between $a_{\text{min}} = 0.005 \mu\text{m}$ and $a_{\text{max}} = 0.2 \mu\text{m}$, which shows that the influence of more complex processes like the dust formation process itself on the model seem to be rather little. A two-component dust composition consisting of 95% OHM warm silicates and 5% DL silicates was found to match the observations best. Assuming a single black-body spectrum for the spectral shape of the central source, it is best represented by a model with $T_{\text{eff}} = 2500$ K. However, moderate variations of T_{eff} only slightly affect the model results. From the best fitting model, we derived a bolometric flux at Earth of $F_{\text{bol}} = 6.99 \times 10^{-11} \text{ W/m}^2$, in accordance with the ISO observational data for the SED at $\Phi_{\text{ISO}} = 0.5 = \Phi_{\text{min}}$. This bolometric flux corresponds to a luminosity of $L = (1.23 \pm 0.12) \times 10^4 L_{\odot}$ at a distance of $D = 2.38 \pm 0.24$ kpc. The radius of the central star is found to be $\vartheta_{\star} = 1.16$ mas or $R \approx 600 R_{\odot}$, and the central-star mass was derived to be $M \approx 1 M_{\odot}$ using the method of Ivezić et al. (1995). Though the density distribution was varied greatly, the general $\rho(r) \propto 1/r^2$ dependence was proven to best fit the observations. The present study matches the observations for a broad wavelength range (from $1 \mu\text{m}$ to $220 \mu\text{m}$).

As regards our visibility at $2.12 \mu\text{m}$, the difference in pulsation phase between the SAO observations and the ISO measurements had to be taken into account. According to the observations, the bolometric flux between the 1996 ISO SED phase and the 2002 SAO visibility phase differs by a factor of 3.3. Therefore, this factor had to be applied to the bolometric flux of the visibility model in order to simultaneously fit the SED and the visibility.

As concerns the study of the parameter space, the grain size turned out to be the key parameter in adjusting the visibility fit while preserving the quality of the SED fit. Both the slope and the curvature of the visibility depend sensitively on the assumed grain radii. The dust mass-loss rate \dot{M} is well constrained by the shape of the SED at longer wavelengths and especially by the shape of the silicate absorption feature. For given optical constants, the value of \dot{M} , as derived from the match of the feature, is not very sensitive to changes in the input parameters. The derived value of $\dot{M} = 2.18 \times 10^{-5} M_{\odot}/\text{yr}$ is of the same order of magnitude as the value of $\dot{M} = 5.58 \times 10^{-5} M_{\odot}/\text{yr}$ given by Heske et al. (1990). The shape of the observed visibility and the strength of the silicate feature constrain the possible grain radii and optical depths of the model, which are found to be the same values that provide the best fit to the SED.

While our model of OH 104.9+2.4 simultaneously fits the observed SED and visibility very well, the modeling included some simplifications. The central source is not a perfect black

body, as the dynamical stellar atmosphere exhibits a complex structure and heterogeneous chemistry. In addition, the feature at $18 \mu\text{m}$ could not be reproduced very well in the SED, due to the simplified dust composition, and the wavelengths above $100 \mu\text{m}$ could only be fitted to a certain extent. This is probably due to the fact that DUSTY allows for the entry of a grain-size distribution, but the code averages dust properties over the entire size distribution before performing any further calculations (see e.g. Wolf 2003). In our case, this leads in particular to an absence of the very large grains found in the tail of the grain-size distribution, which have very high and almost constant absorption and scattering efficiencies. By choosing larger grain sizes, we obtain a much better SED fit for $\lambda \geq 50 \mu\text{m}$, as the emission from the large grains, which have a flatter absorption efficiency and a higher scattering efficiency as smaller grains, then traces the shape of the SED at the long wavelengths, where the dust shell is otherwise optically thin. Unfortunately, this also leads to an optically thin solution for shorter wavelengths due to a lack of small grains, as most of the dust mass is in this case utilized by large grains.

For future considerations, it would be very useful to have additional K -band photometry to secure the derived value for the pulsation phase, as well as photometry in other bands to get better insight into the wavelength dependence of the pulsation amplitude. More visibility measurements, e.g. in the J , H , N , and V bands, would provide additional information on the structure of the dust shell, while additional visibilities in the K' band at another pulsation phase would allow for more detailed conclusions about the response of the dust shell to the variation in the central object, as there may be light-travel time effects involved due to the large scale of the CDS itself.

Acknowledgements. The observations were carried out with the SAO 6 m telescope, operated by the Special Astrophysical Observatory, Russia. Additional NIR photometric data was provided by B. Yudin at the CAO, operated by the Sternberg Astronomical Institute of the Moscow State University, Russia. We thank the Infrared Space Observatory (ISO) operators at the European Space Agency (ESA) for providing the SED data. This research has made use of the SIMBAD database, operated by CDS in Strasbourg, as well as the Gezari catalogue, published by NASA, and the NASA Astrophysics Data System (ADS), operated by NASA. A.B.M. acknowledges support from the Natural Sciences and Engineering Research Council of Canada (NSERC). Finally, we thank the referee, Dr. Peter Woitke, for many helpful comments that stimulated further improvements of the manuscript.

References

- Blöcker, T., Balega, Y., Hofmann, K.-H., et al. 1999, *A&A*, 348, 805
- Blöcker, T., Balega, Y., Hofmann, K.-H., & Weigelt, G. 2001, *A&A*, 369, 142
- Blommaert, J. A. D. L., van der Veen, W. E. C. J., & Habing, H. J. 1993, *A&A*, 267, 39
- Cobb, M. L., & Fix, J. D. 1987, *ApJ*, 315, 325
- Cutri, R. M., Skrutskie, M. F., van Dyk, S., et al. 2003, *VizieR online data catalog*, 2246
- Draine, B. T., & Lee, H. M. 1984, *ApJ*, 285, 89

- Engels, D., Kreysa, E., Schultz, G. V., & Sherwood, W. A. 1983, *A&A*, 124, 123
- Engels, D., Schmid-Burgk, J., & Walmsley, C. M. 1986, *A&A*, 167, 129
- Gauger, A., Balega, Y. Y., Irrgang, P., Osterbart, R., & Weigelt, G. 1999, *A&A*, 346, 505
- Gonzalez-Alfonso, E., Cernicharo, J., Alcolea, J., & Orlandi, M. A. 1998, *A&A*, 334, 1016
- Groenewegen, M. A. T. 1997, *A&A*, 317, 503
- Habing, H. J. 1996, *A&AR*, 7, 97
- Herman, J., & Habing, H. J. 1985, *A&AS*, 59, 523
- Herman, J., Burger, J. H., & Penninx, W. H. 1986, *A&A*, 167, 247
- Heske, A. 1990, *A&A*, 229, 494
- Heske, A., Forveille, T., & Omont, A. 1990, *A&A*, 239, 173
- Höfner, S., Gautschi-Loidl, R., Aringer, B., & Jørgenson, U. G. 2003, *A&A*, 399, 589
- Hofmann, K.-H., Balega, Y., Blöcker, T., & Weigelt, G. 2001, *A&A*, 379, 529
- Ivezić, Z., & Elitzur, M. 1995, *ApJ*, 445, 415
- Ivezić, Z., Nenkova, M., & Elitzur, M. 1999, Internal Report, Univ. of Kentucky
- Jeong, K. S., Winters, J. M., Le Bertre, T., & Sedlmayr, E. 2004, *A&A*, 407, 191
- Jiang, B. W., Deguchi, S., Hu, J. Y., et al. 1997, *AJ*, 113, 1315
- Jones, T. J., Bryja, C. O., Gehrz, R. D., et al. 1990, *ApJS*, 74, 785
- Joyce, R. R., Capps, R. W., Gillett, F. C., et al. 1977, *ApJ*, 213, L125
- Jura, M., & Jacoby, G. 1976, *ApJ*, 18, L5
- Kim, S. H., Martin, P. G., & Hendry, P. D. 1994, *ApJ*, 422, 164
- Knacke, R. F., McCorlke, S., Puetter, R. C., & Erickson, E. 1985, *AJ*, 90, 1828
- Krüger, D., & Sedlmayr, E. 1997, *A&A*, 321, 557
- Labeyrie, C. D. 1970, *A&A*, 6, 85
- Lebofsky, M. J., Kleinmann, S. G., Rieke, G. H., & Low, F. J. 1976, *ApJ*, 206, L157
- Lepine, J. R. D., Ortiz, R., & Epchtein, N. 1995, *A&A*, 299, 453
- Le Squeren, A. M., Sivagnanam, P., Dennefeld, M., & David, P. 1992, *A&A*, 254, 133
- Lorenz-Martins, S., & de Araujo, F. X. 1997, *MNRAS*, 291, 296
- Mathis, J. S., Rumpl, W., & Nordsieck, K. H. 1977, *ApJ*, 217, 425
- Men'shchikov, A. B., Balega, Y. Y., Osterbart, G., & Weigelt, G. 1998, *New Astron.*, 3, 601
- Men'shchikov, A. B., Hofmann, K.-H., & Weigelt, G. 2002b, *A&A*, 392, 921
- Men'shchikov, A. B., Schertl, D., Tuthill, P., Weigelt, G., & Yungelson, L. 2002a, *A&A*, 393, 867
- Merrill, K. M., & Stein, W. A. 1976, *PASP*, 88, 874
- Ney, E. P., & Merrill, K. M. 1980, *AFGL-TR-80-0050*
- Noguchi, K., Qian, Z., Wang, G., & Wang, J. 1993, *PASJ*, 45, 65
- Ossenkopf, V., Henning, T., & Mathis, J. S. 1992, *A&A*, 261, 567
- Pegourie, B. 1988, *A&A*, 194, 335
- Price, S. D., & Murdock, T. L. 1983, *AFGL-TR-83-0161*
- Riechers, D., Driebe, T., Men'shchikov, A. B., & Weigelt, G. 2004, in preparation
- Savage, B. D., & Mathis, J. S. 1979, *ARA&A*, 17, 73
- Schirmacher, V., Woitke, P., & Sedlmayr, E. 2003, *A&A*, 404, 267
- Suh, K.-W. 2002, *MNRAS*, 332, 513
- te Lintel Hekkert, P., Caswell, J. L., Habing, H. J., Haynes, R. F., & Norris, R. P. 1991, *A&AS*, 90, 327
- Welty, A. D., Fix, J. D., & Mutel, R. L. 1987, *ApJ*, 318, 852
- Witt, A. N., Smith, R. K., & Dwek, E. 2001, *ApJ*, 550, L201
- Wolf, S. 2003, *ApJ*, 582, 859
- Xiong, G. Z., Chen, P. S., & Gao, H. 1994, *A&AS*, 108, 661
- Yudin, B. 2003, private communication